Unconventional fabrication of 2D nanostructures and graphene edges

Bellunato, A.

CHAPTER 7

Zero-depth interfacial nanopore capillaries

High-fidelity analysis of translocating biomolecules through nanopores demands shortening the nanocapillary length to a minimal value. Existing nanopores and capillaries, however, inherit a finite length from the parent membranes. Here, nanocapillaries of zero depth are formed by dissolving two superimposed and crossing metallic nanorods, moulded in polymeric slabs. In an electrolyte, the interface shared by the crossing fluidic channels is mathematically of zero thickness and defines the narrowest constriction in the stream of ions through the nanopore device. This novel architecture provides the possibility to design nanopore fluidic channels, particularly with a robust 3D architecture maintaining the ultimate zero thickness geometry independently of the thickness of the fluidic channels. With orders of magnitude reduced biomolecule translocation speed, and lowered electronic and ionic noise compared to nanopores in 2D materials, the findings establish interfacial nanopores as a scalable platform for realizing nanofluidic systems, capable of single-molecule detection.

This chapter was published as a communication: Hadi Arjmandi-Tash, Amedeo Bellunato, Chenyu Wen, René C. Olsthoorn,Ralph H. Scheicher, Shi-Li Zhang, and Grégory F. Schneider. Advanced Materials, 2018, 30, 1703602.

7.1 Introduction

Conventional nanopores are nano-sized fluidic channels drilled across a solid-state membrane[1–6] or moulded in polymeric structures[7,8] and mounted in a flow cell. The flow cell is equally filled with an ionic solution on both sides of the membrane, while a potential difference is applied across the cell serving as the driving force for the ionic transport. Thereby, a flux of ions is established through the nanopore.

Charged molecules can translocate through the nanopore. The instant passage of the molecule momentarily impacts the conductance by locally reducing the aperture size of the channel. The resulting variations of the ionic conductance depends on the local topology of the translocating molecule; particularly, portions of long chain molecules such as polymers, proteins or DNA mark the electronic read-out with specific conductance blockade fingerprints; and ultimately allow for reconstructing the sequence of monomers composing the translocating strands[9].

Consequently, thinner pores, i.e. capillaries with shorter channels, are capable of resolving shorter portions of molecules, leading for instance towards high resolution sequencing devices[1]. Thus, the challenge towards high-resolution sequencing has driven the development of ultra-short channel nanopores. Historically, two major classes of nanopores, i.e. biological and solid state nanopores, have been considered. The thickness of these nanopores varies from a few nanometres, as for α-hemolysin biological nanopores[10,11], up to tens of nanometres for solid-state nanopores[12]. A revolutionary breakthrough aiming at reducing the capillary length of nanopores was achieved by the introduction of two-dimensional (2D) materials such as graphene[13–15], hexagonal boron nitride [16] and molybdenum disulfide[17–20]. Indeed, the monoatomic capillary length of 2D nanopores is expected to offer sequencing capabilities[2], but has not been realized yet. Inferior mechanical stability is one of the downside of thin membranes inherently limiting the sustainability of 2D nanopores. Moreover, the complex fabrication process, involving cleanroom facilities and electron beam lithography[21–23], can be demanding to scale up to industrial production. The noise levels in such devices are also orders of magnitude higher than those for long capillary-based nanopores, thus hindering their application for sequencing[24].

7.2 Results and discussion

To address these issues, we introduce the concept of interfacial nanopores, generated at the crossing of two trenches, as illustrated in Figure 7.1. Fundamentally, the cross-section of two one-dimensional straight lines is a zero-dimensional entity defined as a point (Figure 7.1a). The addition of a second dimensionality implies the overlap of two components to become a surface (Figure 7.1b). Similarly, in a three-dimensional space, the interface shared between two tangent rectangular parallelepipeds is a surface, hence mathematically two-dimensional (Figure 7.1c). Unlike nanopores commonly fabricated in two-dimensional materials – which notwithstanding still possess a finite thickness – the surface defined by the crossing parallelepipeds is strictly two-dimensional and thus does not exhibit any thickness. A negative mould of this structure therefore yields a nanopore with a capillary of length zero (Figure 7.1f).

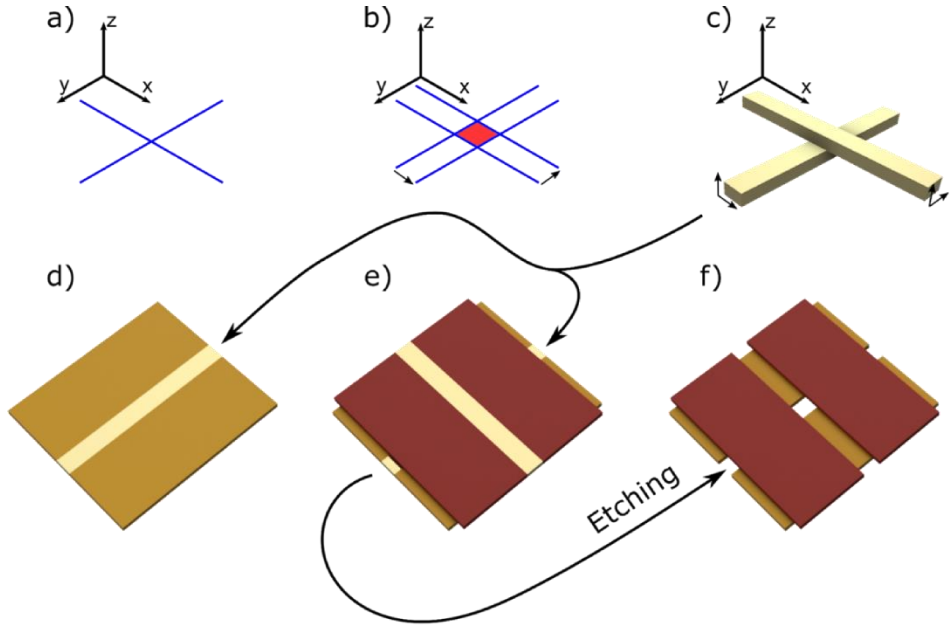

Figure 7.1. Interfacial nanopores: from geometrical concepts to fabrication. a) Zero-dimensional point at the cross-section of two crossing lines. b) 2D lozenge formed at the intersection of two crossing rectangles. c) The lozenge surface is preserved at the interface of two crossing rectangular parallelepipeds. d) A polymeric slab containing a parallelepipedal gold nanorod. e) Stack of two tangent slabs, in a twisted configuration, each containing a rectangular gold parallelepiped nanorod. f) Selective etching of the gold

nanorods with potassium cyanide yielding an interfacial nanopore at the lozenges' interface between the slabs.

In practice, the rectangular parallelepipeds are fabricated by cutting thin (tens of nanometres in thickness) polymeric slabs containing a gold film (Figure 7.1d)[25]. Positioning two of those slabs on top of each other (Figure 7.1e) and selectively etching gold yields the interfacial nanopore (Figure 7.1f). In a typical application, the narrowest constraint in the passage of the buffer solution and ions from one side to the other side of the membrane (two slabs) is of zero thickness.

Atomic force micrographs of the fabricated devices bearing the interfacial nanopore in the middle are shown in Figure 7.2a and 7.2b, respectively before and after dissolving the gold structures. A glass substrate with a microscale opening at the centre was used to provide a mechanical support for the stack of slabs (Figure 7.2c).

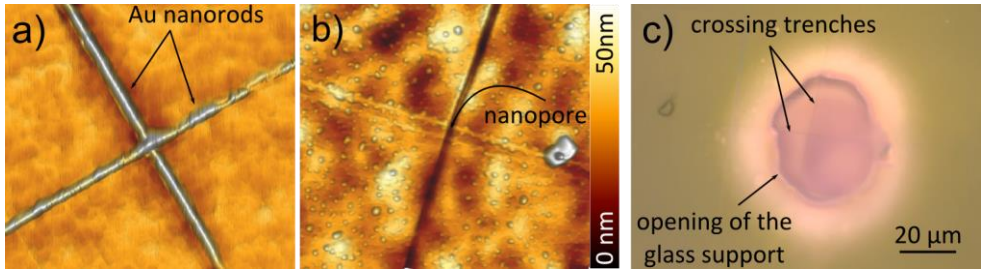

Figure 7.2. AFM characterization. a) Atomic force microscopy image of a two slab stack showing the two tangent-crossing nanorods embedded in the polymeric matrix. b) Atomic force microscopy image of the two slab stack after the etching of the gold using potassium cyanide. The black arrow points toward the nanopore created after the selective etching of the gold nanorods. Both the mappings in (a) and (b) are of 3 µm x 3 µm in size. c) Optical microscopy image of the final structure of a nanopore composed of two slabs, freely standing at the opening of a glass substrate (purple area). The dotted arrows show the lines of the two crossing parallelepipedal trenches.

Figure 7.3a illustrates the I-V characteristic of a nanopore achieved by etching two gold nanorods of 50 nm width and 200 nm height (respectively referred to as *a* and *h* throughout the chapter, see the inset in Figure 7.3b), leading to a pore area of 50×50 nm^2 (see Appendix V for the experimental details). The transmembrane potential sweeps from -200 mV to +200 mV and the salt concentration ranges between 1 mM and 1 M. The linear I-V behaviour confirms the ionic conduction of a nanopore filled with electrolytic solution and allows to exclude the establishment

of any electrochemical reaction within the flow-cell, especially in the proximity of the pore[13–15].

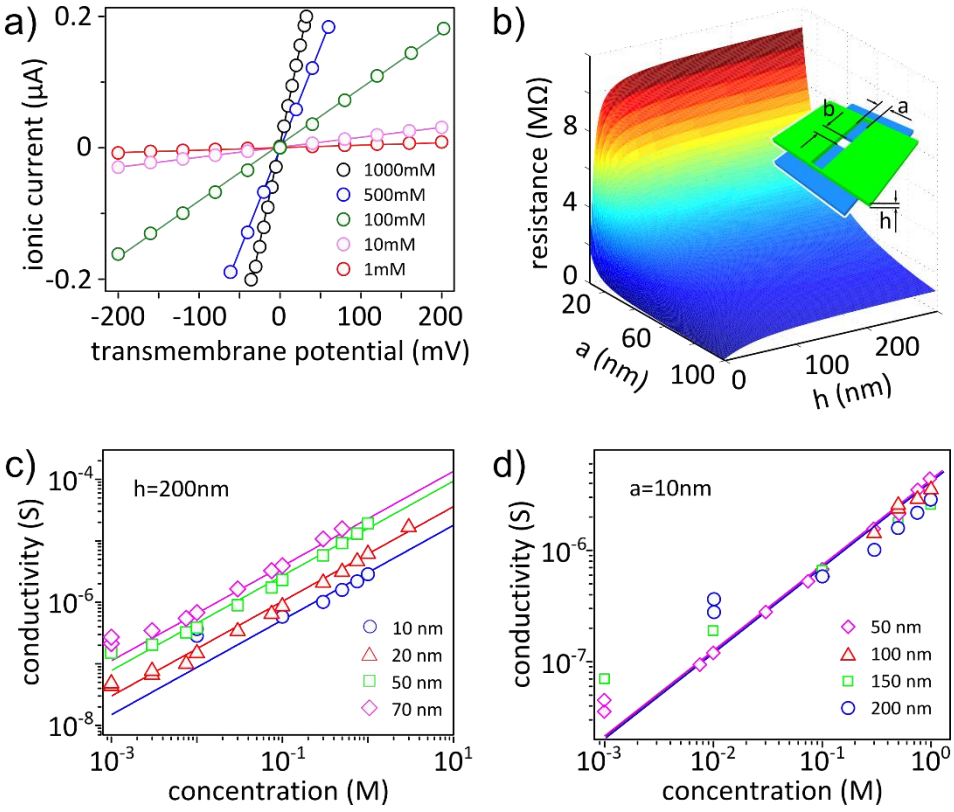

Figure 7.3. Ionic transport through interfacial nanopores. a) Ionic conduction through an interfacial nanopore (*h*=200 nm, *a*=50 nm) upon applying transmembrane potentials in KCl containing buffer solutions of different concentrations**.** b) Theoretically predicted resistance of interfacial nanopores as a function of the trench widths (*a*=*b*) and the equal thickness of the slabs (*h*). The inset depicts the three-dimensional architecture of the interfacial nanopore slab stack. The misorientation angle in between the trenches and the KCl concentration respectively were set to 90° and 1 M in this mapping. c) Conductivity of nanopores of different trench widths (*a*) as a function of the KCl concentration; Slabs of *h* = 200 nm thickness were used to fabricate these nanopores. The continuous lines show the best fittings with equation 1. d) Conductivity of nanopores of different thicknesses of the slabs (*h*) as a function of the KCl concentration; All the samples were of the same trench width of *a* = 10 nm. The continuous lines show the prediction of our model for the conduction and overlap each other.

The ionic flow through conventional nanopores experiences a total resistance due to i) the friction with the channel inside the pore region (pore resistance), and ii)

the convergence of the electric field lines at the 'mouth' of the nanopore (access resistance). Interestingly, the 2D nature of the interfacial nanopore eliminates the pore resistance term. Still, the access resistance of an interfacial nanopore is composed of two terms: i) the access resistance between the reservoir and the channels in the polymeric slabs, and ii) the resistance inside the channel towards the pore, on both sides. Analytically, the overall access resistance (R_t) of an interfacial nanopore is expressed as (see Appendix V):

$$R_t = \gamma \frac{F(a,b,h)}{\pi abqc^n(\mu_+ + \mu_-)} \quad (1)$$

where *c* is the salt concentration in the electrolyte, $q = 1.6 \times 10^{-19}$ C is the elementary charge, μ_+ and μ_- are the mobility of cations and anions, *a* and *b* are the width of the upper and lower channels and *h* is the equal thickness of the slabs (inset in Figure 7.3b). *F* is a function of the geometrical parameters explained in Appendix V. The fitting parameters *γ* and *n* are introduced to take into account the surface conductivity of the pore upon the formation of an electrical double layer, which may impact on the linearity of the I-V curves.

Based on the model in Equation 1, Figure 7.3b provides a mapping for the expected resistance of the nanopore upon changing the geometrical parameters *a* and *h* (here *a* = *b*). The dependency of the resistance on the trench width is normally stronger than on the slab thickness; particularly for $h > 80\ nm$, the resistance is almost independent of *h.*

We experimentally measured the conductance of interfacial nanopores with different trench widths ranging from 10 nm up to 70 nm (Figure 7.3c). As expected, increasing *a* lowers the resistance due to the diffusion of ions leading to increased conductances in widened trenches. In Figure 7.3c, the continuous lines representing the prediction of the model in Equation 1 match with the experimental results for KCl concentrations above 1 mM. As expected, at lower KCl concentrations – and similarly to conventional solid-state nanopores – surface charges on the channel walls yield higher conductances than the one predicted by our model[26,27]. Remarkably and as predicted (Figure 7.3b), the effect of the slab thickness on the measured ionic resistance is negligible, most particularly for slabs thicker than tens of nanometres for ionic strengths above 10 mM (Figure 7.3d).

Again, at lower salt concentrations surface charges add-up to the total conductance of the nanopore architecture.

Figure 7.4a shows a typical time trace of the ionic current through an interfacial nanopore (a = 70 nm, h = 50 nm) immersed in a 5 mM LiCl buffer solution. Upon addition of 48.5 kbp λ-DNA molecules, a series of drops in the conductance of the nanopore appears, depicting the translocation of DNA molecules through the nanopore. Translocation was verified by a polymerase chain reaction (PCR) experiment (See Appendix V).

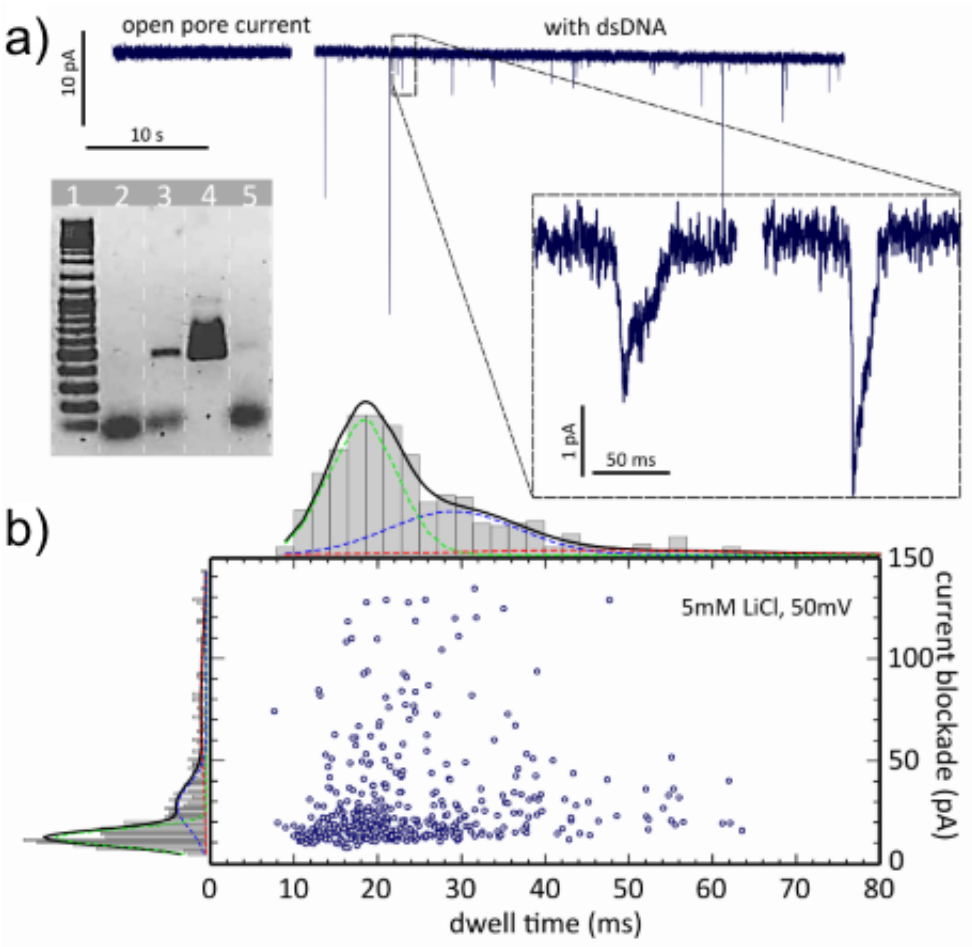

Figure 7.4. Interfacial nanopore as a single molecule sensor. a) Time-trace of the ionic current before and after the injection of λ-DNA (48.5 kbp) to the *cis* chamber of an interfacial nanopore (*a*=50nm, *h*=50nm). The measurement was performed in 5mM LiCl

buffer solution under the application of 30 mV transmembrane potential. The base line current approaches 1.23 nA and the trace is plotted after applying a low-pass filter ($f_{th} = 1\ kHz$). The right inset zooms on two translocation events. The left inset shows the result of the polymerase chain reaction (PCR) experiment where lanes 1, 2, 3, 4, and 5 respectively refer to the DNA marker, lambda DNA present in trans chamber before the translocation, lambda DNA present in trans chamber after translocation, 3 pg λ-DNA and water used as positive and negative controls for PCR (see Appendix V for the experimental details). b) Scatter plot of the amplitude of the current blockade versus translocation time for DNA translocation events through the same nanopore as in (a). The plot features ~400 translocation events, recorded during 10 min of experiments with λ-DNA at a concentration of 10 ng/μl. The distributions of the dwell time and current blockade are separately plotted in left and top inset panels. The dashed lines represent the fits of the events to Gaussian functions.

The duration and blockade current of the translocation events (~400 events) are plotted in Figure 7.4b. Two highly-populated events with Gaussian distributions are identified in both histograms (green and blue dashed curves) that can be attributed to the translocation of DNA molecules with different foldings. The more populated component exhibits an average translocation duration of ~22 ms which corresponds to ~450 ns/bp. Interestingly the measured dwell time is 1.5 to ~100 times longer than the reports for two-dimensional (5 ns/bp[14] - 56 ns/bp [2]), biological (30 ns/bp[28]) and solid-state (40 ns/bp - 300 ns/bp) nanopores[29].

Several observations suggest the presence of a strong interaction between DNA and the walls of the trench, which eventually slows down the translocation of molecules. First, the majority of the translocation events in interfacial nanopores starts sharply but ends smoothly (Figure 7.4a). This observation can be well explained considering a binding mechanism between DNA and the walls of the trench; in fact, the binding requires time and energy to break, in order to let the DNA exit the nanopore (Appendix V). Second, increasing the salt concentration lowers the dwell time through interfacial nanopores (Appendix V). This observation is in striking contrast to the reported behaviour of DNA in SiNx nanopores[29] in which the strong binding between Li^+ to DNA suppresses the translocation speed in high salt concentrations and can be well explained by considering the DNA-nanopore interaction. Third, the widely spread event duration, ranging from less than ~14 ms to over 80 ms (Figure 7.4b), is another signature of the DNA-nanopore interaction: in the absence of such interaction, DNA molecules are expected to exhibit uniform translocations[30]. Hydrophobic interaction between DNA and the

trench walls or cross-over from base-base pi-stacking to base-polymer pi-stacking[31] may govern the DNA-wall interaction.

The ionic resistance of nanopores, generally, is intuitively dominated by that of the most restrictive point (e.g. the interface region for interfacial nanopores) where the electric field is the strongest. Thus, the effective thickness of the nanopore can be defined by referring to the profile of the electric field along the central axis perpendicular to the nanopore area (Appendix V). Specifically, the effective thickness is twice the distance from the nanopore centre to the point where the electric field intensity drops to 1/e of its peak value. According to this definition, the effective thickness of interfacial nanopores with varied slab thicknesses is compared with that of conventional nanopores in Figure 7.5a. We recall the discussion from an earlier section where while ionic resistance in conventional nanopores consists of two components (pore and access resistances), the zero-geometrical thickness (as opposed to the effective thickness) of interfacial nanopores suppresses any contribution of the pore resistance. Indeed, interfacial nanopores show obvious advantages (lower effective nanopore thickness) over conventional nanopores with the channel thicknesses larger than the nanopore size ($h > a$). Our simulations show that the channel length (the thickness of the membrane) governs the effective thickness of conventional nanopores (Appendix V).

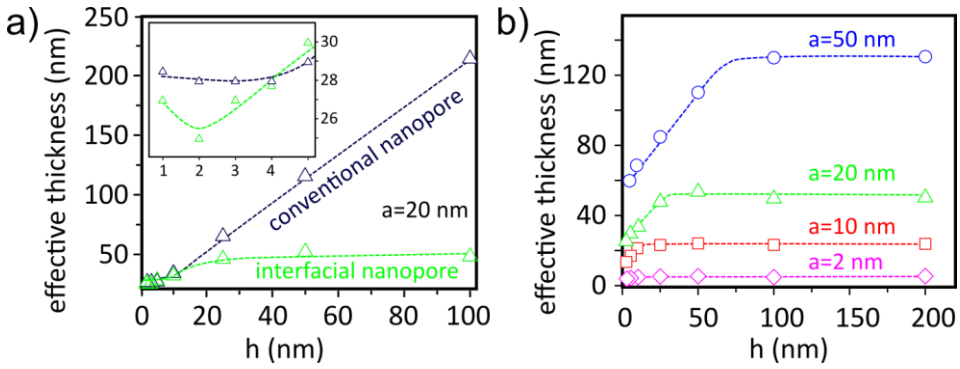

Figure 7.5. Effective thickness of the interfacial nanopores. a) Comparison of the calculated effective thickness of interfacial and conventional nanopores at different thicknesses: The membrane thickness of the conventional nanopore is *2h* to be comparable with interfacial nanopore formed by stacking two membranes, each having the thickness h. Both the nanopores are of squared shape openings of $20\ nm \times 20\ nm$. The inset focuses on a small window at very low h. The vertical and horizontal axis of the inset figure have the same

unit of the main panel. b) Evolution of the effective thickness of interfacial nanopores calculated for different slab thicknesses *h* and nanopore diameters *a*.

In the other extreme ($h < a$, comparable to the typical geometry of 2D nanopores) the effective thickness on each side of the interfacial nanopores can be estimated as half the width of the trench, $a/2$. This estimation resembles the conventional picture of the access resistance in single circular nanopores as two hemispheres with radius $r = d/2$ (where d is the diameter of the nanopore) at each side of the membrane[32,33]. Here, the interfacial nanopores are clearly advantageous since due to the lack of any pore resistance, its effective thickness always falls below that of the conventional nanopores (sum of the access and pore region, inset 7.5a).

As is demonstrated by our simulations (inset and main panel in Figure 7.5a), a conventional nanopore of h = 4 nm is preferred over the one of h = 100 nm as the former provides an effective thickness of ~8 times smaller (higher resolution); but at the same time, such a thin membrane is of poor stability. Hence, a thickness of few tens of nanometres provides a compromise between resolution and stability; this may partially explain why most of the conventional nanopores in solid state materials[34–37] have been sculpted in membranes with a thicknesses of ~ 20 nm. The introduction of interfacial nanopores dramatically shifts this compromise: here the effective thickness of a nanopore with h = 100 nm is just ~1.7 times higher than that of h = 4 nm; hence much thicker nanopores can be chosen without losing the resolution considerably. This is an intriguing property of the interfacial nanopores as the thickness of the membrane and the effective thickness (resolution) are now disentangled. The design of interfacial nanopores is unique as it eliminates the pore thickness; the remaining access resistance term can be minimized by optimizing the geometrical parameters (lowering the area of the pore, Figure 7.5b). Then the design allows to reach an ultimate resolution which is not reachable with conventional designs, always having a finite pore thickness. We note that the experimental evidences for an ultimate resolution can be achieved only when biomolecule sequencing is performed; this is not the case so far as prominent experimental challenges including high translocation speed of molecules do not allow single base reading[2].

Figure 7.6a compares the noise power spectral densities (PSD, denoted by S_I) of three types of nanopores, including a nanopore in graphene, a nanopore in SiNx and an interfacial nanopore, all of similar ionic conductances and comparable

nanopore areas. We used here 1 M KCl to be able to compare the noise of interfacial nanopores with previous reports[14,24]. The parasitic capacitive coupling of the fluidic chambers highly depends on the dielectric constant of the buffer and of the thickness of membrane separating the *cis* and *trans* fluidic reservoirs. The use of a borosilicate-glass support with millimetre thickness lowers the capacitance across the sample: the high frequency noise of the interfacial nanopores is at least one order of magnitude lower compared to conventional nanopores. Yet similar to that of the long channel SiNx nanopores, the maximum low frequency noise of interfacial nanopores is considerably lower than the one in 2D nanopores: the normalized PSD measured at 1 Hz with the current squared $\left(C_{1Hz} = \frac{S_{I,1Hz}}{I^2}\right)$ for twelve different interfacial nanopores at 100 mV transmembrane potential shows a normal distribution centered at $C_{1Hz} = 1.7 \times 10^{-7}$, well comparable to (~4 times higher than) in SiNx nanopores (4.4×10^{-8}) and almost 40 times lower than in 2D nanopores (6.3×10^{-6}) if measured under similar conditions[24] (Figure 7.6b). In fact, evaluating C_{1Hz} is a common approach to compare the noise among different nanopore devices[24].

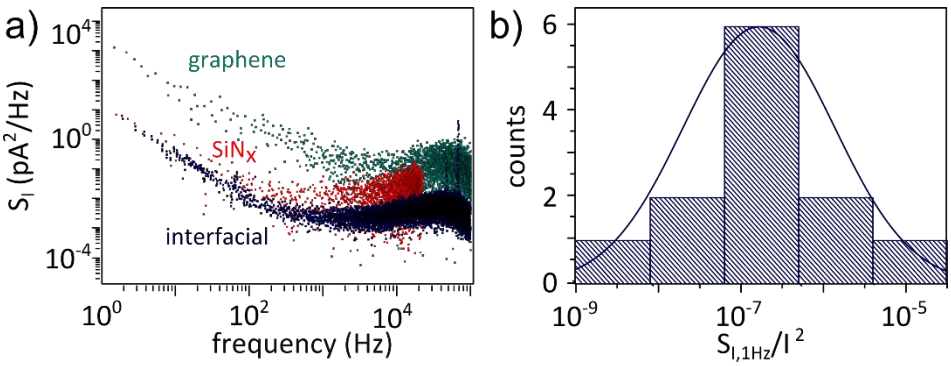

Figure 7.6. Characterization of the noise in interfacial nanopores. a) Comparison of the noise power spectral densities (PSD) of nanopores in graphene ($d = 14.2\ nm$, $R = 9.1\ M\Omega$), in SiNx membrane ($d = 20\ nm, t = 30\ nm, R = 7.5\ M\Omega$), and in an interfacial nanopore (a: $20\ nm, h$: $300\ nm, R = 9.9\ M\Omega$): All the measurements were performed in a 1M KCl buffer solution and under a 100 mV transmembrane potential. b) Distribution of the noise power (at $f = 1Hz$) of interfacial nanopores: measurements performed with 1M KCl buffer solution and under a 100 mV transmembrane potential. Data from 12 different samples with diverse geometries ($100\ nm \leq h \leq 300\ nm$ and $10\ nm \leq a \leq 70\ nm$) were used. Solid line is the Gaussian fit for the distribution.

At frequencies below 1 kHz, a wide variety of nanoscale devices exhibit flicker noise[38], characterized by PSDs exponentially decaying with the frequency: $S_I \propto \frac{1}{f^{\alpha}}$. For the majority of the nanopores studied so far[24,35,38], $\alpha = 1$, hence the low frequency noise is dubbed as $^1/_f$ noise. At commonly used transmembrane potentials (≤200 mV), however, the PSD in the interfacial nanopores, surprisingly exhibits a stronger dependency on frequency as $^1/_{f^2}$ (i.e. $\alpha = 2$). Considerably increasing the potential, however, invokes the $^1/_f$ noise characteristics in the interfacial nanopores (Figure 7.7a). As the origin of the $^1/_f$ noise in conventional nanopores is yet unclear[2,24], understanding the factors altering the noise-frequency dependency in interfacial nanopores are complex, a fortiori (See Appendix V).

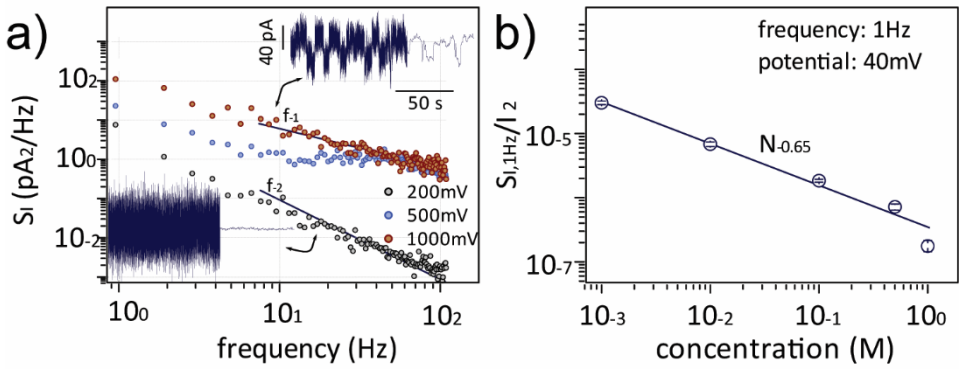

Figure 7.7. Low frequency noise of interfacial nanopores. a) Low frequency noise in an interfacial nanopore ($h = 250\ nm, a = 50\ nm$) at three different transmembrane potentials: Lines with f^{-1} and f^{-2} dependencies are superimposed to the data. Top and bottom insets show the corresponding signals in time-domain (right side low-pass filtered at 1 kHz), respectively measured at 1V and 200mV. The same horizontal and vertical scale bars apply for both of the traces. b) Noise power at $f = 1\ Hz$ as the function of KCl concentration: The data were extracted from 19 different samples with diverse geometries ($50\ nm \leq h \leq 300\ nm$ and $10\ nm \leq a \leq 70\ nm$) under 40mV transmembrane potential. The dotted line shows the best fitting of the data with $C^{-0.65}$.

The low frequency noise in solid-state and biological nanopores obeys Hooge's empirical relation[24,35,36,39] in which the normalized PSD is inversely proportional to the number of charge carriers, $C_{1Hz} \propto N^{-1}$. The model, however, ceases to explain the low frequency noise in graphene [24] and in interfacial nanopores (See Appendix V). We collected $S_I(f = 1\ Hz)$ for 19 different samples (with diverse a and h

values) at various KCl concentrations and plotted against the corresponding squared currents upon applying a constant 40 mV transmembrane potential, Figure 7.7b (see Appendix V). Interestingly, the data corresponding to each concentration level (regardless of the geometry) follows the lines of certain slopes that can be best fitted by $\frac{S_{I,1Hz}}{I^2} \propto N^{-0.65\pm0.05}$. The measured dependency is weaker than the Hoog's prediction, yet stronger than what was observed for graphene nanopores ($\propto N^{-0.27}$)[24].

7.3 Conclusions

In summary, nanopore sensors lacking a capillary depth showed the successful detection of translocating DNA molecules. Compared to the different nanopores studied so far, interfacial nanopores combine an absolute minimal channel length with outstanding mechanical stability, minimum noise level, and reduced translocation rates. The fabrication of interfacial nanopores is scalable and does not require high-level precision. Furthermore, taking advantage of the two nanogaps as potential masks directly aligned with a nanopore, the sandwiching of 2D materials in between the slabs will allow the realization of – for example – graphene nanogap[40] electrodes in a straightforward manner. Future improvements focusing on reducing even further the nanogap widths with alternative parallelepipedal templates will provide insights into sequencing applications with tunnelling currents, an application never achieved hitherto, primarily because of the challenging nanofabrication considerations.

7.4 References

(1) Schneider, G. F.; Dekker, C. *Nat. Biotechnol.* **2012**, *30* (4), 326–328.

(2) Arjmandi-Tash, H.; Belyaeva, L. A.; Schneider, G. F. *Chem. Soc. Rev.* **2016**, *45* (3), 476–493.

(3) Venkatesan, B. M.; Bashir, R. *Nat. Nanotechnol.* **2011**, *6* (10), 615–624.

(4) Kowalczyk, S. W.; Blosser, T. R.; Dekker, C. *Trends Biotechnol.* **2011**, *29* (12), 607–614.

(5) Dekker, C. *Nat. Nanotechnol.* **2007**, *2*, 209–215.

(6) Kim, M. J.; Wanunu, M.; Bell, D. C.; Meller, A. *Adv. Mater.* **2006**, *18* (23), 3149–3153.

(7) Sen, Y. H.; Karnik, R. *Anal. Bioanal. Chem.* **2009**, *394* (2), 437–446.

(8) Jain, T.; Guerrero, R. J. S.; Aguilar, C. A.; Karnik, R. *Anal. Chem.* **2013**, *85* (8), 3871–3878.

(9) Sathe, C.; Zou, X.; Leburton, J.-P.; Schulten, K. *ACS Nano* **2011**, *5* (11), 8842–8851.

(10) Cherf, G. M.; Lieberman, K. R.; Rashid, H.; Lam, C. E.; Karplus, K.; Akeson, M. *Nat. Biotechnol.* **2012**, *30* (4), 344–348.

(11) Song, L.; Hobaugh, M. R.; Shustak, C.; Cheley, S.; Bayley, H.; Gouaux, J. E. *Science.* **1996**, *274* (5294), 1859–1865.

(12) Venkatesan, B. M.; Dorvel, B.; Yemenicioglu, S.; Watkins, N.; Petrov, I.; Bashir, R. *Adv. Mater.* **2009**, *21* (27), 2771–2776.

(13) Schneider, G. F.; Kowalczyk, S. W.; Calado, V. E.; Pandraud, G.; Zandbergen, H. W.; Vandersypen, L. M. K.; Dekker, C. *Nano Lett.* **2010**, *10* (8), 3163–3167.

(14) Merchant, C. A.; Healy, K.; Wanunu, M.; Ray, V.; Peterman, N.; Bartel, J.; Fischbein, M. D.; Venta, K.; Luo, Z.; Johnson, A. T. C.; Drndić, M.; et al. *Nano Lett.* **2010**, *10* (8), 2915–2921.

(15) Garaj, S.; Hubbard, W.; Reina, A.; Kong, J.; Branton, D.; Golovchenko, J. a. *Nature* **2010**, *467* (7312), 190–193.

(16) Zhou, Z.; Hu, Y.; Wang, H.; Xu, Z.; Wang, W.; Bai, X.; Shan, X.; Lu, X. *Sci. Rep.* **2013**, *3*, 3287.

(17) Barati Farimani, A.; Min, K.; Aluru, N. R. *ACS Nano* **2014**, *8* (8), 7914–7922.

(18) Waduge, P. *ACS Nano* **2015**, *9* (7), 7352–7359.

(19) Liu, K.; Feng, J.; Kis, A.; Radenovic, A. *ACS Nano* **2014**, *8* (3), 2504–2511.

(20) Feng, J.; Liu, K.; Bulushev, R. D.; Khlybov, S.; Dumcenco, D.; Kis, A.; Radenovic, A. *Nat. Nanotechnol.* ***2015****, 10, 1070–1076*.

(21) Traversi, F.; Raillon, C.; Benameur, S. M.; Liu, K.; Khlybov, S.; Tosun, M.; Krasnozhon, D.; Kis, A.; Radenovic, A. *Nat. Nanotechnol.* **2013**, *8* (12), 939–945.

(22) Fischbein, M. D.; Drndi, M., Appl. Phys. Lett. **2008**, 93, 113107.

(23) Liu, S.; Lu, B.; Zhao, Q.; Li, J.; Gao, T.; Chen, Y.; Zhang, Y.; Liu, Z.; Fan, Z.; Yang, F.; You, L.; Yu, D. *Adv. Mater.* **2013**, *25*, 4549–4554.

(24) Heerema, S. J.; Schneider, G. F.; Rozemuller, M.; Vicarelli, L.; Zandbergen, H. W. *Nanotechn.* **2014**, 1–18.

(25) Lipomi, D. J.; Martinez, R. V; Whitesides, G. M. *Angew. Chem. Int. Ed. Engl.* **2011**, *50* (37), 8566–8583.

(26) Stein, D.; Kruithof, M.; Dekker, C. *Phys. Rev. Lett.* **2004**, *93* (3), 035901.

(27) Smeets, R. M. M. R. M. M.; Keyser, U. F. U. F.; Krapf, D.; Wu, M. Y. M. Y.; Nynke, H.; Dekker, C.; Dekker, N. H.; Dekker, C. *Nano Lett.* **2006**, *6* (1), 89–95.

(28) Wanunu, M.; Sutin, J.; McNally, B.; Chow, A.; Meller, A. *Biophys. J.* **2008**, *95* (10), 4716–4725.

(29) Kowalczyk, S. W.; Wells, D. B.; Aksimentiev, A.; Dekker, C. *Nano Lett.* **2012**, *12* (2), 1038–1044.

(30) Garaj, S.; Liu, S.; Golovchenko, J. A.; Branton, D. *Proc. Natl. Acad. Sci.* **2013**, *110* (30), 12192–12196.

(31) Akca, S.; Foroughi, A.; Frochtzwajg, D.; Postma, H. W. C. *PLoS One* **2011**, *6* (4), e18442.

(32) Hall, J. R. *J. Gen. Physiol.* **1975**, *66* (2), 531–532.

(33) Levadny, V.; Aguilella, V. M.; Belaya, M. *Biochim. Biophys. Acta - Biomembr.* **1998**, *1368*, 338–342.

(34) Smeets, R. M. M.; Keyser, U. F.; Wu, M. Y.; Dekker, N. H.; Dekker, C. *Phys. Rev. Lett.* **2006**, *97* (8), 088101.

(35) Smeets, R. M. M.; Dekker, N. H.; Dekker, C. *Nanotechnology* **2009**, *20* (9), 095501.

(36) Smeets, R. M. M.; Keyser, U. F.; Dekker, N. H.; Dekker, C. *Proc. Natl. Acad. Sci. U. S. A.* **2008**, *105* (2), 417–421.

(37) Kowalczyk, S. W.; Hall, A. R.; Dekker, C. *Nano Lett.* **2010**, *10* (1), 324–328.

(38) Balandin, A. *Nat. Nanotechnol.* **2013**, *8* (8), 549–555.

(39) Bezrukov, S. M.; Vodyanoy, I.; *Biomembrane Electrochemistry*; **1994**; 375–399.

(40) Postma, H. W. C. *Nano Lett.* **2010**, *10* (2), 420–425.